Real-space pseudopotential method for calculating magnetocrystalline anisotropy

Masahiro Sakurai[1,*] and James R. Chelikowsky[1,2,3,†]
[1]*Center for Computational Materials, Institute for Computational Engineering and Sciences, The University of Texas at Austin, Austin, Texas 78712, USA*
[2]*Department of Chemical Engineering, The University of Texas at Austin, Austin, Texas 78712, USA*
[3]*Department of Physics, The University of Texas at Austin, Austin, Texas 78712, USA*

(Received 17 July 2018; published 24 August 2018)

We present a real-space pseudopotential method for calculating magnetocrystalline anisotropy within relativistic density-functional theory. The spin-orbit interaction, a fundamental origin of magnetocrystalline anisotropy, is incorporated with norm-conserving pseudopotentials expressed on a real-space grid. We demonstrate the utility of our method by calculating the magnetocrystalline anisotropy constant, K_1, of YCo_5, which is a prototype compound with large K_1. Our calculated K_1 agrees with previous theoretical work. We show that our formalism also works for describing magnetocrystalline anisotropy in other transition-metal compounds, such as Mn_2Ga and FeNi, which have modest values for K_1. Our real-space pseudopotential method is well suited for a parallel computing environment and is an efficacious approach to solving the relativistic Kohn-Sham equations, which include spin-orbit effects as well as noncollinear magnetism.

DOI: 10.1103/PhysRevMaterials.2.084411

I. INTRODUCTION

Spin-orbit interactions, a relativistic effect that couples the spin and orbital components of the magnetic moments, induce rich physical phenomena in condensed matter systems. Among the magnetic phenomena arising from the spin-orbit coupling, magnetocrystalline anisotropy is of growing interest in recent years [1]. In particular, high magnetocrystalline anisotropy is an excellent source for yielding large magnetic coercivity, which is a favorable property for permanent magnet materials.

In the presence of the spin-orbit interactions, there are energetically favorable ("easy") and unfavorable ("hard") directions for the magnetization, $\vec{M}$. Suppose a material has an uniaxial magnetic anisotropy; the magnetocrystalline anisotropy energy can be expressed, to the first order, by

$$E(\theta) = K_1 V \sin^2\theta, \tag{1}$$

where θ is the angle between magnetization $\vec{M}$ and the easy axis, and V is the volume of a system. The coefficient K_1 is called the magnetocrystalline anisotropy constant. For tetragonal or hexagonal crystal structures, the magnetocrystalline anisotropy energy can also be given by the total-energy difference between the systems magnetized along the easy and hard axes:

$$E_a = E(\vec{M} \perp \vec{z}) - E(\vec{M} \parallel \vec{z}), \tag{2}$$

with $\vec{z}$ being the easy axis.

Computing the magnetic anisotropy energy E_a from first principles is difficult. A relativistic generalization [2,3] of density-functional theory (DFT) [4,5] makes it possible to describe the spin-orbit effects. However, additional complicated terms in the formalism lead to intense computations. Moreover, the magnetic anisotropy energy E_a is typically of the order of 1 meV per formula unit, requiring high numerical accuracy. Two popular DFT codes, VASP [6,7] and QUANTUM ESPRESSO [8], can run in a "spin-orbit mode" using a plane-wave basis to solve the relativistic Kohn-Sham equation [9–11]. An alternative approach for solving the relativistic Kohn-Sham equation is a real-space method [12,13], which is simple to implement and is well suited for a parallel computing environment, owing to a reduction in global communications such as fast Fourier transforms.

We present a real-space implementation of the relativistic DFT for describing magnetocrystalline anisotropy from first principles. Our real-space approach employs a norm-conserving pseudopotential to incorporate the spin-orbit effects, which are crucial to yielding magnetocrystalline anisotropy. We demonstrate our method by applying it to three prototype compounds including YCo_5. Our results are in good agreement with previous calculations. We also show the efficiency of parallelization schemes used in our real-space DFT code PARSEC.

II. METHODOLOGY

A. Real-space formalism

A real-space formalism can be used to calculate the total energy of a material that is magnetized along the easy (hard) axis. In the presence of spin-orbit coupling, the Hamiltonian can be written as [2,3]

$$\hat{H} = H_0 \hat{I} + \hat{H}^{\mathrm{SO}} + \hat{B}_{\mathrm{xc}} \cdot \vec{\sigma}. \tag{3}$$

The first term represents the Hamiltonian in a standard spin-polarized case. In atomic units ($e = m = \hbar = 1$), we can write this Hamlitonian as

$$H_0 = -\frac{\nabla^2}{2} + V_{\mathrm{ion}} + V_H + V_{\mathrm{xc}}, \tag{4}$$

*masahiro@ices.utexas.edu
†jrc@utexas.edu

where $V_{\rm ion}$ is the ionic pseudopotential. We use norm-conserving pseudopotentials in a separable form [14,15]. V_H is the Hartree potential. $V_{\rm xc}$ is the exchange-correlation potential.

The second term $\hat{H}^{\rm SO}$ accounts for spin-orbit interactions, which are also based on norm-conserving pseudopotentials [16,17].

The third term of Eq. (3), $\hat{B}_{\rm xc}$ is the magnetic exchange-correlation potential, which is given by functional derivative of the exchange-correlation energy functional $E_{\rm xc}$ with respect to the spin density, $\vec{m}(\vec{r})$:

$$\hat{B}_{\rm xc} = \frac{\delta E_{\rm xc}[n, \vec{m}]}{\delta \vec{m}}, \tag{5}$$

where $n(\vec{r})$ is the electronic charge density.

We use a Kohn-Sham two-component spinor wave function $\vec{\Psi}_{n\vec{k}}(\vec{r})$ with band index n and wave vector $\vec{k}$. In Eq. (3), $\hat{I}$ is a 2×2 identity matrix and $\vec{\sigma}$ is a vector of the Pauli matrices.

We expand the Laplacian in real space using high-order finite differences on an orthogonal, uniform grid:

$$\nabla^2\phi(x, y, z) = \frac{1}{h^2}\sum_{n=-N}^{N} C_n[\phi(x + nh, y, z) + \phi(x, y + nh, z) + \phi(x, y, z + nh)], \tag{6}$$

where h is the grid spacing and C_n are the coefficients for Nth order expansion.

The spin-orbit effects are included with norm-conserving pseudopotentials [16,17]. The total ionic pseudopotential $V^{\rm ps}$ can be written as

$$V^{\rm ps}(r) = \sum_{l,m} |l, m\rangle \left[V_l^{\rm ion}(r) + V_l^{\rm SO}(r)\vec{L}\cdot\vec{S}\right]\langle l, m|, \tag{7}$$

with the spherical harmonics $|l, m\rangle$ and the spin-orbit coupling operators

$$\vec{L}\cdot\vec{S} = \hat{L}_z\hat{S}_z + \frac{1}{2}(\hat{L}_+\hat{S}_- + \hat{L}_-\hat{S}_+), \tag{8}$$

where $\hat{L}_\pm = \hat{L}_x \pm i\hat{L}_y$ and $\hat{S}_\pm = \hat{S}_x \pm i\hat{S}_y$. In a manner similar to the Kleinman-Bylander separation technique [14] for the ionic component $V_l^{\rm ion}$, the spin-orbit component $V_l^{\rm SO}$ can also be decomposed into local and nonlocal parts [18]. With some algebra [19], we obtain diagonal and off-diagonal blocks of $V^{\rm ps}$, respectively:

$$V_{\sigma,\sigma}^{\rm ps,nloc} = \sum_{l,m} u_{l,m}u_{l,m}^\dagger + \frac{1}{4}\sum_{l,m}[l(l+1) - m\sigma]v_{l,m}v_{l,m}^\dagger + \frac{1}{2}\sum_{l,m} m\sigma(v_{l,m}u_{l,m}^\dagger + u_{l,m}v_{l,m}^\dagger), \tag{9}$$

and

$$V_{\sigma,\sigma'}^{\rm ps,nloc} = \frac{1}{2}\sum_{l,m}\sqrt{l(l+1) - m(m+\sigma')} \times \left(-\frac{1}{2}v_{l,m+\sigma'}v_{l,m}^\dagger + v_{l,m+\sigma'}u_{l,m}^\dagger + u_{l,m+\sigma'}v_{l,m}^\dagger\right). \tag{10}$$

Here, $\sigma = 1$ (up spin) or -1 (down spin), and $u_{l,m}$ ($v_{l,m}$) is the projected vector of the ionic (spin-orbit) pseudo wave function expressed on a real-space grid. We note that σ' is not equal to σ in Eq. (10). Owing to the presence of the magnetic exchange-correlation term [20,21], the full Hamiltonian has additional diagonal and off-diagonal blocks:

$$\hat{B}_{\rm xc}\cdot\vec{\sigma} = \begin{pmatrix} B_z & B_x - iB_y \\ B_x + iB_y & -B_z \end{pmatrix}. \tag{11}$$

We implemented the above formalism in our real-space pseudopotential DFT code PARSEC [12,13,22].

We first perform scalar-relativistic (SR) [23] calculations by neglecting the second term of Eq. (7). The SR solutions along with an initial magnetization, $\vec{m}_0(\vec{r})$, are then used as an initial guess for solving full Hamiltonian that includes the spin-orbit interactions. With the self-consistent solution to the full Hamiltonian, we obtain the total energy of a material with magnetization along the easy or hard axis.

The Hamiltonian matrix remains sparse, making it feasible to operate matrix-vector multiplications and diagonalizations even though matrix dimension is doubled due to spinor representation. The PARSEC code is suitable for modern many-processor computers as parallel algorithms based on the standard MPI (message passing interface) scheme allow efficient matrix-vector multiplications. The MPI parallelization can also be done over the wave vector k points, which is highly beneficial when the present method is applied to crystalline materials. Iterations during a self-consistent field loop are accelerated by using a Chebyshev subspace filtering method, which emphasizes convergence of the charge density as opposed to individual eigenfunctions [24–26]. We show the efficiency of these parallelization schemes in Sec. III C.

A key aspect of real-space methods is the avoidance of global communications such as fast Fourier transforms. Another advantage of our real-space method is its flexibility in handling different boundary conditions. In our formalism, the generalized Kohn-Sham equations are solved on an equal footing for various boundary conditions. Unlike plane-wave DFT codes, such as VASP and QUANTUM ESPRESSO, our real-space approach does not exploit a supercell technique. As demonstrated in previous work [19,21], real-space methods work well for confined systems as well as two-dimensional materials, where spin-orbit effects and noncollinear magnetism were tested separately. In Sec. III, we will show that our real-space formalism that includes both the spin-orbit effects and the spin density $\vec{m}(\vec{r})$ works for crystalline materials as well.

B. Computational details

We use a generalized-gradient approximation (GGA) functional [27] for the exchange-correlation potential. The polynomial order N of the finite-difference expansion is set to be 6. A grid spacing of 0.3 a.u. (approximately 0.16 Å) is used. A generalized Broyden method [28] is used for mixing old and new potentials. Pseudopotentials are constructed with $s/p/d$ core radii (in a.u.) of 2.35/2.60/2.35 for Mn, 2.20/2.40/2.20 for Fe, 2.18/2.38/2.18 for Co, 2.18/2.38/2.18 for Ni, and 3.19/3.64/3.19 for Y. A partial core correction [29] is included as well. The Monkhorst-Pack scheme [30] is used to generate a k-point grid to perform Brillouin-zone integration.

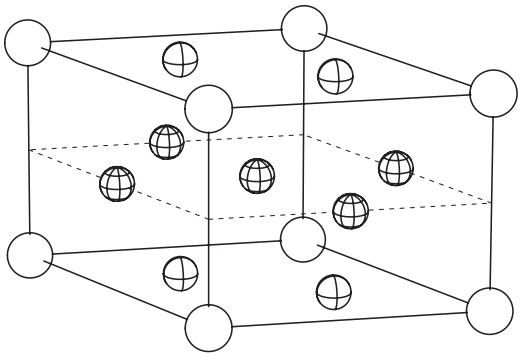

FIG. 1. Crystal structure of the YCo_5 compound. Open and decorated spheres represent Y and Co atoms, respectively. Two inequivalent Wyckoff sites ($2c$ and $3g$) are indicated by different decoration pattern.

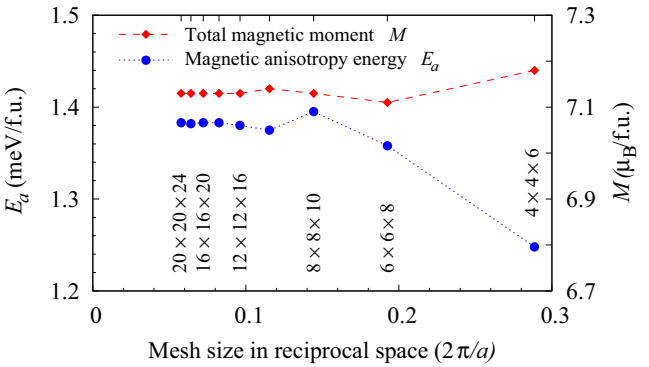

FIG. 2. Convergence of total magnetic moment M and magnetic anisotropy energy E_a of the $P6/mmm$ YCo_5 compound as a function of a mesh size in reciprocal space. The values represent a k-point grid for a particular resolution.

III. RESULTS

A. YCo_5

We demonstrate our real-space implementation by applying our real-space method to YCo_5. The crystal structure of YCo_5, shown in Fig. 1, is a $CaCu_5$-type structure ($P6/mmm$, space group No. 191). The unit cell contains one Y atom at the origin, two Co atoms at the $2c$ site [(1/3, 2/3, 0) and (2/3, 1/3, 0)], and three Co atoms at the $3g$ site [(1/2, 0, 1/2), (0, 1/2, 1/2), and (1/2, 1/2, 1/2)]. The lattice constant is $a = 4.92$ Å and $c/a = 0.80$.

Figure 2 shows the convergence of the total magnetic moment M and the magnetic anisotropy energy E_a of the $P6/mmm$ YCo_5 compound with respect to a k-point mesh. We find that the magnetic anisotropy energy converges much more slowly in comparison to the total magnetic moment. To achieve a better convergence for both M and E_a of the $P6/mmm$ YCo_5 compound requires a fine k-space resolution of $0.8 \times 2\pi/a$, which corresponds to a k-point grid of $14 \times 14 \times 18$.

In Table I, our real-space DFT results are compared with previous calculations [31–33] as well as experiment [1]. The calculated total magnetic moment, $7.13\mu_B$ per YCo_5, is in good agreement with the previous theoretical values. A linear muffin-tin orbital method within atomic-sphere approximation [31] (LMTO-ASA) gave $6.90\mu_B$ per YCo_5, and a full potential version of a linear-augmented plane-wave (FLAPW) method [32] yielded $7.06\mu_B$ per YCo_5. With the calculated total magnetic moment, we estimate magnetic polarization saturation $\mu_0 M_s$ to be 1.01 T, which is very close to the experimental value. The easy magnetization axis for YCo_5 in the $P6/mmm$ structure is correctly determined by the present real-space method. The calculated magnetic anisotropy energy E_a of 1.38 meV per molecular unit of YCo_5 is approximately two times as large as the previous LDA-based value [31]. The difference between the calculated E_a values originates from a choice of exchange-correlation functional as well as the different approaches to evaluate E_a: the force theorem, a single-shot non-self-consistent calculation, is used in Ref. [31], while we used the self-consistent total energies. Our GGA value is comparable to the previous GGA result [32]. From the calculated E_a, we obtain the corresponding K_1 of 2.68 MJ/m^3. Compared to the experimental K_1 of 6.5 MJ/m^3, theory underestimates K_1 by a factor of about 2.

The underestimation of the magnetic anisotropy energy E_a and the corresponding magnetocrystalline anisotropy constant K_1 by DFT-based methods has been reported in earlier work [31]. Computing a more accurate K_1 requires one to go beyond the current approximations to the electron correlations, as demonstrated by recent work [33,34]. For example, combination of the local-density approximation and the dynamical mean-field theory (LDA + DMFT) is shown to give a more accurate K_1 value [33]. However, it remains challenging to determine the strength of the on-site Coulomb interaction U without ambiguity.

B. Mn_2Ga and FeNi

We perform calculations for other compounds based on $3d$ transition metals. We choose Mn_2Ga and FeNi as test cases. These two compounds are among Mn- or Fe-based

TABLE I. Comparison of magnetic properties obtained for the $P6/mmm$ YCo_5 compound: total magnetic moment M, magnetic polarization saturation $\mu_0 M_s$, magnetic anisotropy energy E_a, and magnetocrystalline anisotropy constant K_1. Experimental values are also listed. The E_a value given in parentheses is estimated from the experimental K_1.

Method	M (μ_B/YCo_5)	$\mu_0 M_s$ (T)	E_a (meV/YCo_5)	K_1 (MJ/m^3)
Real-space DFT, GGA (PARSEC)	7.13	1.01	1.38	2.68
LMTO–ASA, LDA [31]	6.90	0.97	0.60	1.16
FLAPW, GGA (WIEN97) [32]	7.06	1.00	1.63	3.16
Experiment [1]		1.06	(3.4)	6.5

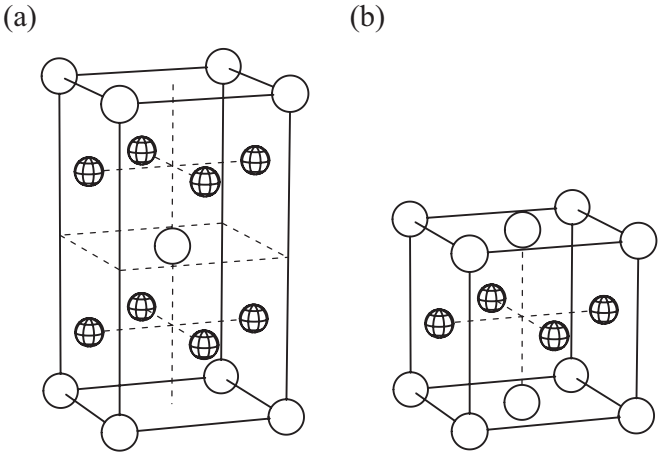

FIG. 3. Crystal structures of (a) $D0_{22}$-type Mn_2Ga and (b) $L1_0$-type FeNi. In Mn_2Ga, Mn atoms (decorated spheres) are located on the faces of the unit cell, while Ga atoms (open spheres) are at the corner and at the body center of the unit cell.

rare-earth-free materials with a potential to provide sufficient magnetic anisotropy and magnetization [1].

Mn_2Ga has an Al_3Ti-type tetragonal $D0_{22}$ structure ($I4/mmm$, space group No. 139) as shown in Fig. 3(a). In spite of its small magnetization, Mn_2Ga provides moderate magnetocrystalline anisotropy of 2.35 MJ/m^3, leading to good coercivity without rare-earth elements [36–38]. We used the experimental lattice constant of $a = 3.905$ and $c = 7.193$ Å.

FeNi is one of the ordered $L1_0$ binary alloys. Its crystal structure ($P4/mmm$, space group No. 123) arises from tetragonal distortion of a perfect fcc structure, as illustrated in Fig. 3(b). FeNi exhibits high magnetization associated with Fe, while its magnetocrystalline anisotropy is as low as 0.7 MJ/m^3 in a single crystalline film [39]. We used the experimental lattice constant of $a = 3.93$ and $c = 3.56$ Å.

We perform these calculations with a fine momentum-space resolution of $0.625 \times 2\pi/a$ to ensure convergence. This resolution corresponds to a k-point grid of $16 \times 16 \times 8$ ($16 \times 16 \times 16$) for Mn_2Ga (FeNi).

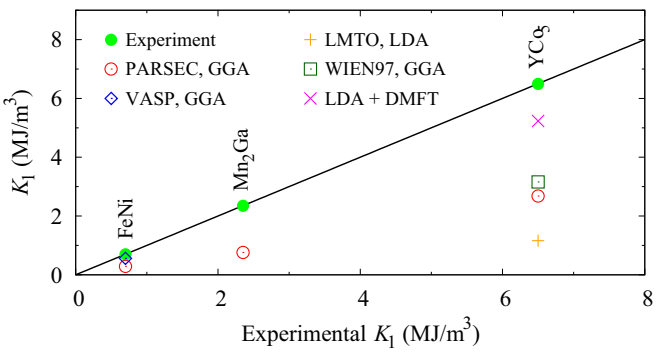

FIG. 4. Comparison of calculated magnetocrystalline anisotropy constants K_1 from our method (PARSEC) and from other theoretical approaches [31–33,35] with experimentally determined K_1 for the FeNi, Mn_2Ga, and YCo_5 compounds.

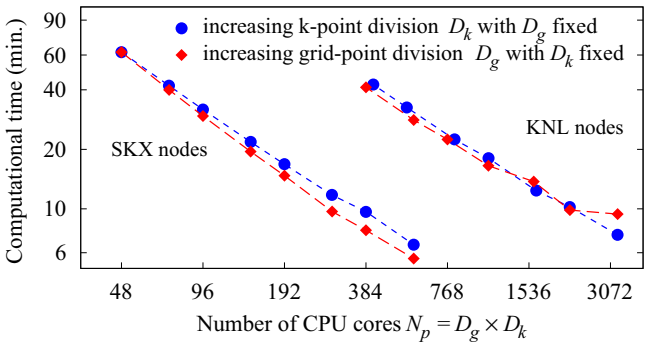

FIG. 5. Computational time vs the number of CPU cores used for example YCo_5 calculations performed on the Stampede2 supercomputer at the Texas Advanced Computing Center. Both the horizontal and vertical axes are in logarithmic scale. Grid points and k points, divided by D_g and D_k, respectively, are distributed over $N_p (= D_g \times D_k)$ processors.

Figure 4 compares the magnetocrystalline anisotropy constants K_1 calculated by our real-space method (PARSEC) and by other approaches [31–33,35] with experimentally determined K_1 for the FeNi, Mn_2Ga, and YCo_5 compounds. Our K_1 value for FeNi is consistent with the previous GGA-based value using the VASP code [35]. Again, K_1 for FeNi and Mn_2Ga is underestimated by a factor of 2–3, which is quite similar to the case of YCo_5.

C. Parallelization

We show the efficiency of parallelization schemes implemented in our real-space code PARSEC. Example calculations on YCo_5 were performed on Stampede2, the flagship supercomputer at the Texas Advanced Computing Center [40], where "SKX" compute nodes are equipped with two 24-core Intel Xeon Platinum 8160 ("Skylake") processors, a total of 48 CPU cores per node. Stampede2 also hosts "KNL" compute nodes that feature 68-core Intel Xeon Phi 7250 ("Knights Landing") processors.

The number of iterations needed to achieve self-consistency varies with a k-point grid used. To make a fair comparison, we measured computational time spent for the first 20 steps that include Chebyshev-Davidson diagonalization at the first step and subsequent subspace filtering steps. Figure 5 shows the results on example YCo_5 calculations, where 576 irreducible k points, generated from a $12 \times 12 \times 16$ k-point grid, can be computed in parallel. In PARSEC, grid points can also be distributed through out processors, forming an additional layer of parallelization. In sending and receiving the data between neighboring processors, we utilize a nonblocking mechanism (the MPI_IALLREDUCE routine) in order to hide latency due to communications. It it evident in Fig. 5 that computational time drops linearly with respect to k-point division as well as grid-point division. Computational cost scales linearly on both SKX and KNL nodes with up to thousands of CPU cores, indicating transferability of our code on different computing architectures.

IV. SUMMARY

We describe a real-space pseudopotential method for calculating the magnetic anisotropy of a material. Our real-space code (PARSEC) is used to solve the electronic structure using pseudopotentials constructed with density-functional theory. PARSEC is explicitly designed for an efficient implementation on a parallel computing system. We successfully applied the code to prototypical compounds—YCo_5, Mn_2Ga, and FeNi—yielding an accurate magnetization and a magnetocrystalline anisotropy constant consistent with other density-functional methods.

ACKNOWLEDGMENTS

The authors would like to thank Leeor Kronik for helpful discussions. We acknowledge support from a grant from the NSF, Grant No. DMREF-1729202. High-performance computing resources were provided by the Texas Advanced Computing Center (TACC) at The University of Texas at Austin as part of the Extreme Science and Engineering Discovery Environment (XSEDE), which is supported by the NSF, Grant No. ACI-1548562, through XSEDE Allocation No. MCA08X029.

[1] R. Skomski and J. M. D. Coey, Scr. Mater. **112**, 3 (2016).
[2] A. K. Rajagopal and J. Callaway, Phys. Rev. B **7**, 1912 (1973).
[3] A. H. MacDonald and S. H. Vosko, J. Phys. C **12**, 2977 (1979).
[4] P. Hohenberg and W. Kohn, Phys. Rev. **136**, B864 (1964).
[5] W. Kohn and L. J. Sham, Phys. Rev. **140**, A1133 (1965).
[6] G. Kresse and J. Furthmüller, Comput. Mater. Sci. **6**, 15 (1996).
[7] G. Kresse and J. Furthmüller, Phys. Rev. B **54**, 11169 (1996).
[8] P. Giannozzi, S. Baroni, N. Bonini, M. Calandra, R. Car, C. Cavazzoni, D. Ceresoli, G. L. Chiarotti, M. Cococcioni, I. Dabo, A. D. Corso, S. de Gironcoli, S. Fabris, G. Fratesi, R. Gebauer, U. Gerstmann, C. Gougoussis, A. Kokalj, M. Lazzeri, L. Martin-Samos, N. Marzari, F. Mauri, R. Mazzarello, S. Paolini, A. Pasquarello, L. Paulatto, C. Sbraccia, S. Scandolo, G. Sclauzero, A. P. Seitsonen, A. Smogunov, P. Umari, and R. M. Wentzcovitch, J. Phys.: Condens. Matter **21**, 395502 (2009).
[9] G. Kresse and D. Joubert, Phys. Rev. B **59**, 1758 (1999).
[10] A. Dal Corso and A. Mosca Conte, Phys. Rev. B **71**, 115106 (2005).
[11] A. Dal Corso, Phys. Rev. B **82**, 075116 (2010).
[12] J. R. Chelikowsky, N. Troullier, and Y. Saad, Phys. Rev. Lett. **72**, 1240 (1994).
[13] J. R. Chelikowsky, N. Troullier, K. Wu, and Y. Saad, Phys. Rev. B **50**, 11355 (1994).
[14] L. Kleinman and D. M. Bylander, Phys. Rev. Lett. **48**, 1425 (1982).
[15] N. Troullier and J. L. Martins, Phys. Rev. B **43**, 1993 (1991).
[16] L. Kleinman, Phys. Rev. B **21**, 2630 (1980).
[17] G. B. Bachelet and M. Schlüter, Phys. Rev. B **25**, 2103 (1982).
[18] L. A. Hemstreet, C. Y. Fong, and J. S. Nelson, Phys. Rev. B **47**, 4238 (1993).
[19] D. Naveh, L. Kronik, M. L. Tiago, and J. R. Chelikowsky, Phys. Rev. B **76**, 153407 (2007).
[20] U. von Barth and L. Hedin, J. Phys. C **5**, 1629 (1972).
[21] D. Naveh and L. Kronik, Solid State Commun. **149**, 177 (2009).
[22] L. Kronik, A. Makmal, M. L. Tiago, M. M. G. Alemany, M. Jain, X. Huang, Y. Saad, and J. R. Chelikowsky, Phys. Status Solidi B **243**, 1063 (2006).
[23] D. D. Koelling and B. N. Harmon, J. Phys. C **10**, 3107 (1977).
[24] Y. Zhou, Y. Saad, M. L. Tiago, and J. R. Chelikowsky, Phys. Rev. E **74**, 066704 (2006).
[25] Y. Zhou, Y. Saad, M. L. Tiago, and J. R. Chelikowsky, J. Comput. Phys. **219**, 172 (2006).
[26] Y. Zhou, J. R. Chelikowsky, and Y. Saad, J. Comput. Phys. **274**, 770 (2014).
[27] J. P. Perdew, K. Burke, and M. Ernzerhof, Phys. Rev. Lett. **77**, 3865 (1996).
[28] V. Eyert, J. Comput. Phys. **124**, 271 (1996).
[29] S. G. Louie, S. Froyen, and M. L. Cohen, Phys. Rev. B **26**, 1738 (1982).
[30] H. J. Monkhorst and J. D. Pack, Phys. Rev. B **13**, 5188 (1976).
[31] G. H. O. Daalderop, P. J. Kelly, and M. F. H. Schuurmans, Phys. Rev. B **53**, 14415 (1996).
[32] P. Larson and I. Mazin, J. Magn. Magn. Mater. **264**, 7 (2003).
[33] J.-X. Zhu, M. Janoschek, R. Rosenberg, F. Ronning, J. D. Thompson, M. A. Torrez, E. D. Bauer, and C. D. Batista, Phys. Rev. X **4**, 021027 (2014).
[34] M. C. Nguyen, Y. Yao, C.-Z. Wang, K.-M. Ho, and V. P. Antropov, J. Phys.: Condens. Matter **30**, 195801 (2018).
[35] Y. Miura, S. Ozaki, Y. Kuwahara, M. Tsujikawa, K. Abe, and M. Shirai, J. Phys.: Condens. Matter **25**, 106005 (2013).
[36] J. Winterlik, B. Balke, G. H. Fecher, C. Felser, M. C. M. Alves, F. Bernardi, and J. Morais, Phys. Rev. B **77**, 054406 (2008).
[37] M. Jamer, B. Assaf, S. Bennett, L. Lewis, and D. Heiman, J. Magn. Magn. Mater. **358-359**, 259 (2014).
[38] A. A. El-Gendy and G. C. Hadjipanayis, J. Phys. Chem. C **119**, 8898 (2015).
[39] T. Shima, M. Okamura, S. Mitani, and K. Takanashi, in Proceedings of the 17th International Conference on Magnetism [J. Magn. Magn. Mater. **310**, 2213 (2007)].
[40] http://www.tacc.utexas.edu.